Bifurcation Analysis of Surge and Rotating Stall in the Moore-Greitzer Compression System

Csaba Hős*
hoscsaba@vizgep.bme.hu

Alan Champneys†
a.r.champneys@bris.ac.uk

László Kullmann‡
kullmann@vizgep.bme.hu

September 5, 2002

Abstract

A simple compression system model, described by a set of three ordinary nonlinear differential equations (the Moore-Greitzer model) is studied using bifurcation analysis to give a qualitative understanding of the presence of surge and rotating stall. Firstly, three parameter values are chosen and a reduced planar system is studied to detect the local bifurcations of pure surge modes. The global bifurcation diagrams are then completed with the help of the continuation software AUTO. A special feature of this 2D system is a set of parameter values where two Takens-Bogdanov points merge. As a next step, the interaction of surge and rotating stall modes is analysed using the same branch tracking technique. Several novel bifurcation scenarios are described. Two-parameter bifurcation maps are computed and a satisfactory agreement with experimental results is found. An explanation is given for the onset of deep surge, rotating stall, classic surge and the hysteresis effects experienced in measurements.

1 Introduction

Compression systems are widely used in engineering applications, such as e.g. turbojet engines, air conditioning systems, industrial compressors (see [5]). The function of turbomachines (such as fans or compressors) in these systems is to increase the pressure of the fluid and they are designed to operate in steady axisymmetric flow. As one decreases the mass flow rate through the turbomachine, the pressure rise increases and this improves the performance. However, below a critical value of mass flow rate, the steady design flow is no longer stable and oscillations occur, whose main types can be classified as (deep) surge, rotating stall and classic surge.

Roughly speaking, surge is a large-amplitude, low-frequency (compared to rotating stall) oscillation of the total, annulus-averaged mass flow rate and may be encountered in both fan and compressor systems. The vibration can be so severe that the flow reverses for a part of the period, which is often called deep surge. Rotating stall is an abrupt fall of pressure rise below a critical mass flow rate associated with the rotation of one or several stalled blade passages around the annulus, and is typically present in axial compressors. In this case, one finds that the annulus-averaged mass flow rate remains constant in time. Classic surge is a combination of surge and rotating stall, when during a surge cycle, the compressor passes in and out of rotating stall. All of these instabilities limit the operation severely and may lead to large penalties in performance. Hence, there has been an extensive search for a low-order model capable of describing the essential of the dynamics in order to gain a parametric understanding of how to avoid these instabilities. The model due to E.M. Greitzer in 1976 showed a satisfactory agreement between numerical experiments and measurements (see [11]), although the compressor characteristic was assumed a priori to be a piecewise

*Department of Hydraulic Machines, Budapest Uni. of Technology and Economics (BME), 1521 Budapest, Pf. 91, Hungary
†Department of Engineering Mathematics, Uni. of Bristol, Queen's Building, University Walk, Bristol, BS8 1TR, England
‡Department of Hydraulic Machines, BME

smooth function with built-in hysteresis. Ten years later, Greitzer and Moore introduced an improved model in [22] equipped with a smooth cubic polynomial characteristic, in which the rotating stall equilibrium appeared as a separate branch of fixed points, existing for a limited range of parameter values. This study triggered the idea that surge and rotating stall can be modelled independently from each other, though, both in numerical simulations and laboratory experiments they often occur combined.

Since these two pioneering articles, further studies have been published which approach the problem in different ways; in the light of nonlinear bifurcation theory (see e.g. [21],[1],[2]) or linear/nonlinear control methods (see e.g. [9], [15], [4], [8]). (The interested reader should also refer to the review articles [12] and [13]). The utility of bifurcation analysis was first realized by McCaugham [21], where the third-order Moore-Greitzer model was studied with the powerful numerical continuation software AUTO [7]. This direction of research was further developed and combined with control theory by Abed et al. (see [1], [2], [20]), Chen et al. [4] and the more recent paper of Wang and Murray [23]. Let us also mention the work [24] by Xiao and Basar, in which they proved the existence of a two-dimensional centre manifold of the viscous Moore-Greitzer partial differential equation (PDE) model and showed the existence of a Hopf bifurcation. However, we believe that there are some features of the behaviour of the original, uncontrolled equations, which are not yet described in the literature. Also, although the two-parameter bifurcation analysis carried out by McCaughan (see Fig.16 in [21]) shows good agreement with the experimentally determined 'stability chart' by Moore and Greitzer (Fig.19 in [11]), there are missing features, notably an explanation for the large rotating stall/surge hysteresis found experimentally in a wide parameter range. Furthermore, we would like to demonstrate the strength and efficiency of numerical continuation techniques which allow us to find those parameter values, at which global bifurcations occur, which we show to play a key role in the dynamics of the system and yet cannot be detected by conventional (linear) stability analysis.

With the help of continuation software, not only the location and stability of the fixed points can be tracked, but also periodic solutions (either stable or unstable) and their (global) bifurcations (e.g. homoclinic connections, bifurcations of limit cycles) can be detected and continued in the parameter space. Another important benefit of global bifurcation analysis is that it reveals those parameter ranges, where although the fixed point is (locally) stable, it coexists with another stable limit cycle or a more complex attractor, which is easily missed by linear techniques. Examples will be given e.g. of coexisting (a) uniform-flow operating point and surge, (b) rotating stall and deep surge and (c) rotating stall and classic surge. This allows us to refine the stability boundaries obtained by linear stability analysis.

This paper is organized as follows. After defining the model in §2, we start in §3 by studying pure surge modes via a reduced, planar model. Two new parameters are introduced; the first one allows us to describe a more general turbomachine characteristic while the second one ('opening pressure') helps us to generalize the throttle characteristic. This change results in the possibility of several (one, two or three) coexisting fixed points (for the analysis of several fixed points, see also [2]). Then, by linear stability analysis, we determine the domain of local stability and also detect the basic kinds of stability losses, namely, fold (or saddle-node), Hopf and Bogdanov-Takens bifurcation. By carrying out the Hopf normal form transformation, analytical first-order approximations to the amplitude and frequency of the surge cycle are given. Then, using AUTO, a complete two-parameter bifurcation diagram is described, paying special attention to the case of three operating points, which involves a series of homoclinic bifurcations to hyperbolic and non-hyperbolic equilibria. The results of this section can be applied to fan and pump systems as well, where rotating stall is not expected to occur. Having completed the analysis of the pure-surge case, in §4 we turn our attention to rotating stall and combined stall-surge modes. The interaction between the three basic modes (deep surge, rotating stall and classic surge) is explained in one-parameter bifurcation diagrams, while also a two-parameter bifurcation map is presented and compared to the experimentally determined one in [11]. Evidence is found of complex dynamics due to a novel Shil'nikov-like homoclinic orbit to a non-hyperbolic equilibrium. The transition from one mode to another is carefully explained, which also gives a qualitative answer to the issue of hysteresis.

2 Governing Equations

The Moore-Greitzer model [22] consists of a compressor (fan) working in an annular duct, which is connected to an exit plenum of much larger diameter. The discharge from the plenum is then via a throttle in an exit

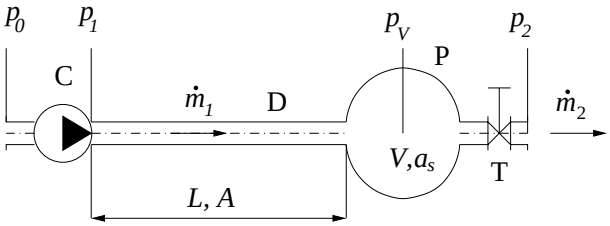

Figure 1: Theoretical compression system, fluid with ambient pressure p_0 flows through compressor C, duct D of cross-section area A and length L, and plenum P with volume V and sonic velocity a_S before exiting through throttle T to exhaust space with constant pressure $p_2 \geq p_0$. All non-displayed pipe lengths are assumed to be infinitesimal compared with L.

duct whose diameter is again much smaller than that of the plenum. It is important that the exit duct must be short so that the kinetic energy of the gas inside can be neglected (see Fig.1). Let us assume that the flow in the pipe is one-dimensional, incompressible, without friction. Then, by applying the unsteady Bernoulli equation, the change of mass flow rate can be expressed as

$$\frac{d\dot{m}_1}{dt} = \frac{A}{L}(p_1 - p_V), \tag{2.1}$$

where $\dot{m}_1$ $[\frac{kg}{m^3}]$ is the mass flow rate, $p_1 - p_V$ [Pa] is the pressure difference between the two ends of the pipe, A $[m^2]$ stands for the flow-through area and L [m] is the length of the pipe. Let us suppose that the plenum is big enough to assume that the pressure along the space coordinate does not vary and the gas inside is at rest. In this case, the mass balance of the plenum can be written as

$$\frac{d(\rho V)}{dt} = \dot{m}_1 - \dot{m}_2, \tag{2.2}$$

where ρ $[\frac{kg}{m^3}]$ is the density of the gas, and V $[m^3]$ is the volume of the plenum and $\dot{m}_1$, $\dot{m}_2$ $[\frac{kg}{s}]$ are the mass flow rates entering and leaving the plenum per unit time, respectively. If we use as a reference velocity the fan revolution speed u and a time-scale parameter ω_H (Helmholtz-frequency) defined as

$$\omega_H = a_s\sqrt{\frac{A}{VL}}, \tag{2.3}$$

then (2.1) becomes

$$\frac{d\Phi}{d\tau} = B(\Psi_1 - \Psi_2), \tag{2.4}$$

where a_S is the sonic velocity, Φ is the non-dimensional mass flow rate, Ψ is the non-dimensional pressure, $\tau = \omega_H\, t$ and B is the (also dimensionless) Greitzer-parameter, defined as

$$B = \frac{u}{2L\omega_H}. \tag{2.5}$$

Note that B depends only on the geometry of the system, for a given compressor characteristic (e.g. constant revolution speed u) it is independent of the operating point. Using the dimensionless state variables defined above, assuming that the density is a function of pressure only (i.e. $\rho = \rho(p)$) and that the process in the plenum is polytropic, (2.2) turns into

$$\frac{d\Psi}{d\tau} = \frac{1}{B}(\Phi_1 - \Phi_2). \tag{2.6}$$

The losses in the system are concentrated into the throttle, whose static characteristic is assumed to be valid in dynamical operation as well. If we apply the orifice equation and use the dimensionless state variables Φ and Ψ, the mass flow rate through the throttle can be written as

$$\Psi_T(\Phi_T) = \gamma_{T0} + \frac{1}{\gamma_T^2}\Phi_T^2, \tag{2.7}$$

where Ψ_T is the (dimensionless) pressure drop through the valve, Φ_T is the mass flow rate through the valve, γ_{T0} is the pressure drop corresponding to zero mass flow rate ('opening pressure') and γ_T is proportional to the flow-through area inside the orifice. Finally, the turbomachine (fan, compressor, pump), is described by its static characteristic, which is assumed to be valid under dynamical operation and may be approximated by a cubic polynomial of the form (following the original notation of Greitzer in [11])

$$\Psi_C(\Phi) = \Psi_{C0} + H\left(1 + \frac{3}{2}\left(\frac{\Phi - \Phi_0}{W} - 1\right) - \frac{1}{2}\left(\frac{\Phi - \Phi_0}{W} - 1\right)^3\right). \tag{2.8}$$

Comparing (2.7) and (2.8) with those found in the literature, one should notice that two new parameters were introduced, namely Φ_0 and γ_{T0}. The first one, Φ_0 is simply a shift along the Φ axis and gives us the possibility to describe the shape of the compressor characteristic more generally and, together with γ_{T0}, will allow us to study the dynamics of three, coexisting equilibria. Introducing γ_{T0} is reasonable from an engineering perspective as well, as in real compression systems, the turbomachine often has to overcome a constant overpressure (denoted by $p_2 - p_0$ in Fig.1) at all mass flow rates.

Taking into account that the inlet pressure of the pipe is the pressure rise of the compressor, the mass flow rate leaving the pipe is the same as the one entering the plenum and that the exhaust from the plenum is via the throttle, the governing equations yield

$$\begin{aligned} \Phi' &= B(\Psi_C(\Phi) - \Psi_V) \\ \Psi' &= \frac{1}{B}\left(\Phi - \gamma_T\sqrt{\Psi_V - \gamma_{T0}}\right), \end{aligned} \tag{2.9}$$

where $' = \frac{d}{d\tau}$.

System (2.9) describes surge completely but does not include rotating stall. The extension needed is derived and explained in detail in [22], here we present the main idea and the resulting system only. Mass and pressure balance considerations of the compressor and the overall compression system lead to a set of three nonlinear partial differential equations (Moore-Greitzer PDE system). One-mode truncation via Galerkin projection gives the third-order set of ordinary differential equations given by system (59)-(61) in [22]. The new variable J which appears represents the square root of the amplitude of the first Galerkin mode. Due to the different time scalings in (2.9) and the Moore-Greitzer system in [22], one cannot see directly that the latter is an extension of (2.9). To keep the analysis coherent and make the results comparable, the following rescaling and assumptions are made: dimensionless time $\zeta = \frac{u}{R}$ is replaced by dimensionless time τ defined through the Helmholtz-frequency (see eq.(2.3)) and l_I (inlet pipe length of the compressor) and l_T (overall outlet pipe length of the plenum) are neglected (the latter also implies $m = 1$ in eq.(61) in [22]). The resulting system can be written as

$$\begin{aligned} \Phi' &= C\left[\Psi_C(\Phi, J) - \Psi_V\right] \\ \Psi' &= \frac{C}{4B^2}\left[\Phi - \gamma_T\sqrt{\Psi_V - \gamma_{T0}}\right] \\ J' &= J\rho\left[1 - \left(\frac{\Phi}{W} - 1\right)^2 - \frac{1}{4}J\right], \end{aligned} \tag{2.10}$$

where

$$\begin{aligned} C &= \frac{1}{l_C}\frac{u}{R\,\omega_H}, \\ B &= \frac{u}{2\,L\,\omega_H}, \\ \rho &= \frac{3H}{W}\frac{a}{1+a}\frac{u}{R\,\omega_H} \\ l_C &= \frac{1}{a} + \frac{L}{R} \quad \text{and} \\ a &= \frac{R}{N\,T\,u}, \end{aligned}$$

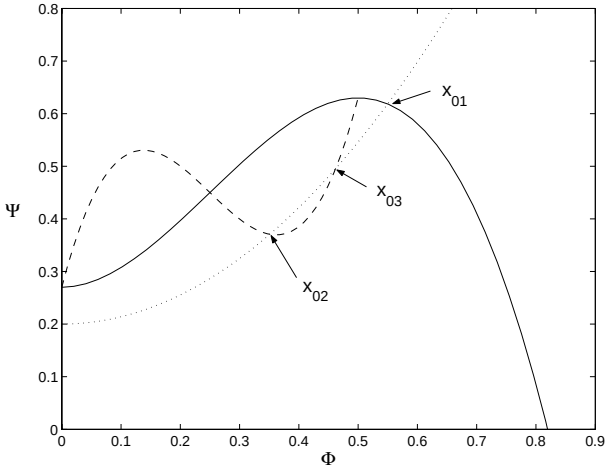

Figure 2: Unstalled (solid line) and stalled (dashed line) compressor and throttle (dotted line) characteristic. Operating points x_{02} and x_{03} are stalled ($J \neq 0$) while x_{01} is unstalled. Parameter values used to plot: $H = 0.18$, $W = 0.25$, $\Psi_0 = 0.27$, $\Phi_0 = 0.0$, $\gamma_{T0} = 0.2$ and $\gamma_T = 0.85$.

with new parameters; N compressor stages, T compressor time lag, l_C total aerodynamical length of the pipe measured in radii of the annulus, R radius of the annulus and a reciprocal time-lag parameter of blade passage. The presence of rotating stall influences the compressor characteristic and following Greitzer and Moore, for $\Phi_0 = 0$, the characteristic will be given by

$$\Psi_C(\Phi, J) = \Psi_{C0} + H\left(1 + \frac{3}{2}\left(\frac{\Phi}{W} - 1\right)\left(1 - \frac{1}{2}J\right) - \frac{1}{2}\left(\frac{\Phi}{W} - 1\right)^3\right). \tag{2.11}$$

If $J = 0$ and $\Phi_0 = 0$, (2.11) turns into (2.8), while for $J \neq 0$ one obtains the 'stalled' characteristic. Note that if $T \to 0$ (i.e. the compressor is modelled by its *static* characteristic), we have $C \to 2B$ and, if $J = 0$ is set, we regain the stall-free equations given by system (2.9) (apart from the small - formal - difference that we have to replace B by $2B$, which is due to the original scalings in [22]). Hence, the model that includes rotating stall is indeed a straightforward extension of the system describing pure surge.

Before plunging into the analysis, let us briefly summarize some aspects of system (2.10), already known from the literature. System (2.10) has two types of fixed points; (a) rotating stall-free ($J_e = 0$) and (b) rotating stall fixed points: $J_e^{RS} = 4 - 4\left(\frac{\Phi}{W} - 1\right)^2$. Substituting J_e^{RS} into (2.11) one obtains the 'stalled' characteristic of the compressor (see Fig.2), with the remarkable result that it is qualitatively similar to those obtained by laboratory experiments, especially the sudden and steep drop around $\Phi = 2W$. This suggests that (roughly speaking) the compressors have a smooth 'stall-free' characteristic (solid line in Fig.2), but the operating point located on this segment may be unstable while the other, 'stalled' fixed point is stable, as shown in [21]. Hence, one would never be able to measure experimentally the stall-free segment of the characteristic after the stall limit. The $J = 0$ plane is invariant (trajectories starting there cannot escape). Also, the phase space is bounded 'above' by $J = 4$ as in this case, $J' \leq 0$ for all Φ values. Moreover, as J represents the square root of the amplitude of the first-order harmonic of rotating stall, it has to be positive, so we restrict our attention to the region $0 \leq J \leq 4$. The phase space is divided into two parts by the parabola given by $J = 4 - 4\left(\frac{\Phi}{W} - 1\right)^2$. Between the two arms of this parabola, $J' > 0$ (the rotating-stall component is increasing), while in the outer region $J' < 0$. As a consequence, the $J = 0$ plane is (weakly) repelling if $0 \leq \Phi \leq 2W$ and (weakly) attracting otherwise.

3 Pure Surge

Let us study the onset of surge and the post-surge behaviour. Pure surge is often encountered in fan systems, a stability analysis can be found in [17] and experimental verifications in [18] or [10]. In this case, the flow after the turbomachine remains axisymmetric, but there is a large-amplitude, low-frequency vibration of the annulus-averaged mass flow. From now on, we assume the compressor characteristic to be fixed and concentrate on the remaining three parameters: γ_{T0}, γ_T and B. The first two determine the location of the operating point while Greitzer's parameter B has a fundamental effect on the dynamics, both at local and global scales.

3.1 Linear Stability Analysis

To obtain a first, local view on the system's dynamical behaviour, we investigate the neighbourhood of the fixed points (Φ_e, Ψ_e), which are the roots of the cubic polynomial equation

$$\Psi_e = \Psi_C(\Phi_e) = \gamma_{T0} + \frac{1}{\gamma_T^2}\Phi_e^2. \tag{3.1}$$

Let us introduce the notation for more then one fixed point: $\Phi_e^{(1)} \leq \Phi_e^{(2)} \leq \Phi_e^{(3)}$ to avoid latter confusion. By introducing the new variable $\mathbf{x} = col(x_1, x_2) \stackrel{\text{def}}{=} col(\Phi - \Phi_e, \Psi - \Psi_e)$, system (2.9) turns into

$$\mathbf{x}' = \mathbf{A}\,\mathbf{x} + \mathbf{F}(\mathbf{x}), \tag{3.2}$$

with

$$\mathbf{A} = \begin{pmatrix} B\alpha_1 & -B \\ \frac{1}{B} & -\frac{1}{B\beta_1} \end{pmatrix} \quad \text{and} \quad \mathbf{F}(\mathbf{x}) = \begin{pmatrix} B\alpha_2 x_1^2 + B\alpha_3 x_1^3 \\ -\frac{\beta_2}{B}x_2^2 - \frac{\beta_3}{B}x_2^3 + h.o.t. \end{pmatrix}, \tag{3.3}$$

in which

$$\begin{array}{lll} \alpha_1 = \frac{3H}{2W}\left[1 - \left(\frac{\Phi_e - \Phi_0}{W} - 1\right)^2\right] & \alpha_2 = \frac{3H}{2W^2}\left(1 - \frac{\Phi_e - \Phi_0}{W}\right) & \alpha_3 = -\frac{H}{2W^3} \\ \beta_1 = \frac{2}{\gamma_T}\left(\Psi_e - \gamma_{T0}\right)^{\frac{1}{2}} & \beta_2 = -\frac{\gamma_T}{8}\left(\Psi_e - \gamma_{T0}\right)^{-\frac{3}{2}} & \beta_3 = \frac{\gamma_T}{16}\left(\Psi_e - \gamma_{T0}\right)^{-\frac{5}{2}}. \end{array} \tag{3.4}$$

Note that α_1 and β_1 represent the slope of the compressor and throttle characteristics respectively, evaluated at the operating point. The local behaviour of the system near the fixed point is governed by the eigenvalues of the linear coefficient matrix $\mathbf{A}$ and we have a qualitative change in the phase portrait whenever the real part of an eigenvalue vanishes. Simple calculation shows that when crossing the line $\beta_1 = \alpha_1$, one of the purely real eigenvalues vanishes (fold or saddle-node bifurcation, i.e. the birth - or death - of a pair of new fixed points), while along the hyperbola $\beta_1 = (B^2\alpha_1)^{-1}$, a pair of complex conjugate eigenvalues cross the imaginary axes (Hopf bifurcation, birth of a limit cycle). It is easy to show that at the point $\tilde{\alpha}_1 = \tilde{\beta}_1 = B^{-1}$, the hyperbola is normal to the line (corresponding to fold bifurcation), hence, both eigenvalues are zero, which is a Bogdanov-Takens (or double-zero) bifurcation and a complete new curve corresponding to a saddle homoclinic bifurcation originates at this point (for details see e.g. [19]). The results of linear stability analysis are sketched in Fig.3.

3.2 Fold bifurcation

Finding the branches in the original $(\gamma_T, \gamma_{T0}, B)$ parameter space corresponding to fold bifurcations will allow us to decide the number of coexisting fixed points. This can be achieved by searching for those parameter values, at which equation (3.1) has exactly two solutions. Using the standard technique to solve a cubic polynomial equation, this curve can be given implicitly as a function of γ_{T0} and γ_T or, alternatively, one can use AUTO to compute it. The result is shown in Fig.4. The critical value of γ_{T0}, below which fold bifurcation cannot occur can be calculated analytically, in our case it turns out to be 0.2343 (the corresponding value of γ_T is 0.7422); at these values a cusp bifurcation occurs. One may check briefly that the eigenvalues along the fold branch are given by $\lambda_1 = 0$ and $\lambda_2 = B\alpha_1 - \frac{1}{B\alpha_1}$.

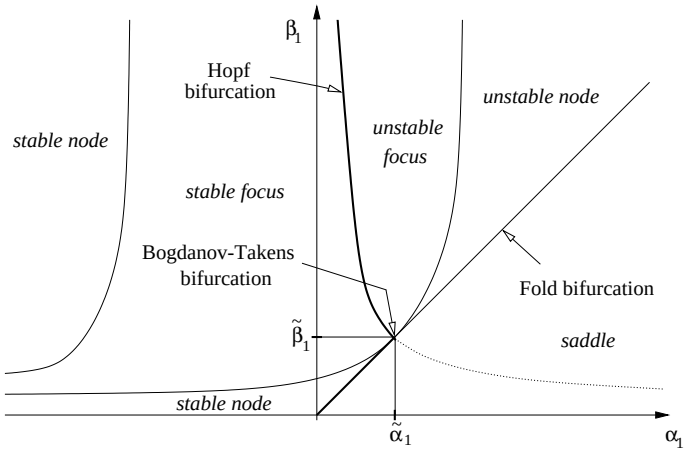

Figure 3: Result of the linear stability analysis (see text for details). The linear stability region is to the left of the bold line.

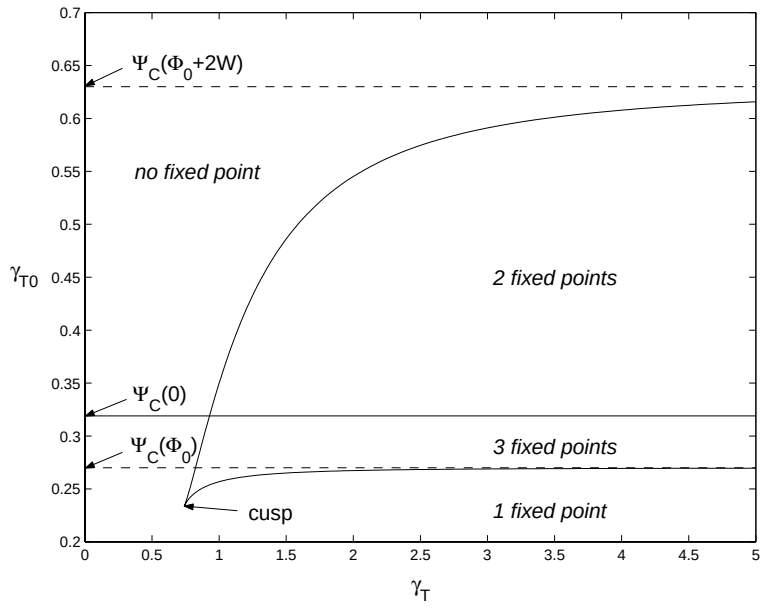

Figure 4: Fold bifurcation on parameter plane (γ_T, γ_{T0}) showing the cusp at (0.7422,0.2343). (Parameter values: $H = 0.18$, $W = 0.25$, $\Psi_{C0} = 0.27$, $\Phi_0 = 0.1$, B is arbitrary.)

3.3 Hopf bifurcation

At the Hopf bifurcation we have a pair of complex conjugate eigenvalues crossing the imaginary axes with non-zero velocity as a parameter varies. In this case, a periodic orbit is born around the fixed point, which is obviously our candidate to grow into a surge cycle. To analyse the bifurcation in detail, we carry out the Hopf normal form transformation in order to give first-order approximation to the amplitude and frequency of the limit cycle and to determine its stability. Recall that if the conditions

$$\beta_{1,crit} = \frac{1}{B^2\alpha_1} \quad \text{and} \quad |B\alpha_1| < 1 \tag{3.5}$$

are fulfilled, we have a pair of purely imaginary eigenvalues, given by

$$\lambda_{1,2} = \pm i\omega = \pm i\sqrt{1 - B^2\alpha_1^2}. \tag{3.6}$$

The speed of the eigenvalues crossing the imaginary axis with variation of β_1 is non-zero, as

$$d = \frac{d}{d\beta_1}\Re(\lambda)\bigg|_{\beta_1=\beta_{1,crit}} = \frac{1}{2}B^3\alpha_1^2. \tag{3.7}$$

Following the method described in [14] or [19], let us define the new coordinates $\mathbf{y} = col(y_1, y_2)$ via the transformation $\mathbf{x} = \mathbf{T}\,\mathbf{y}$, where the columns of $\mathbf{T}$ are composed by the real and imaginary part of the eigenvectors corresponding to the critical eigenvalues, i.e.

$$\mathbf{T} = \begin{pmatrix} \Re(s_1) & \Im(s_1) \end{pmatrix} = \begin{pmatrix} B^2\alpha_1 & B\omega \\ 1 & 0 \end{pmatrix}. \tag{3.8}$$

Substituting this into (3.2), we arrive at the system

$$\begin{pmatrix} \dot{y}_1 \\ \dot{y}_2 \end{pmatrix} = \begin{pmatrix} 0 & \omega \\ -\omega & 0 \end{pmatrix} \begin{pmatrix} y_1 \\ y_2 \end{pmatrix} + \begin{pmatrix} f(y_1, y_2) \\ g(y_1, y_2) \end{pmatrix}, \tag{3.9}$$

and it is easy to calculate the important parameter (first Lyapunov coefficient)

$$\begin{aligned} a \;=\; & \frac{1}{16}\left[f_{30} + f_{12} + g_{21} + g_{03}\right] + \frac{1}{16\omega}\left[f_{11}\left(f_{20} + f_{02}\right) - g_{11}\left(g_{20} + g_{02}\right)\right. \\ & \left. - f_{20}g_{20} + f_{02}g_{02}\right] = \frac{\alpha_1}{4B\omega^2}\left(\beta_2^2 - B^6\alpha_2^2\right) + \frac{3}{8B}\left(B^4\alpha_3 - \beta_3\right), \end{aligned} \tag{3.10}$$

where $f_{ij} = \frac{\partial^{i+j} f}{\partial y_1^i \partial y_2^j}$ and all the coefficients in a and d are evaluated at the critical parameter values (for details, see [14] or [19]). Finally, the approximation of the amplitude of the limit cycle can be written as

$$r = \sqrt{-\frac{d}{a}\left(\beta_1 - \beta_{1,crit}\right)}, \tag{3.11}$$

and, after transforming back the result into the original (x_1, x_2) plane, we are left with

$$x_1(t) = B\,r\,\sin(\omega\tau + \phi) \quad \text{and} \quad x_2(t) = r\,\cos(\omega\tau), \tag{3.12}$$

where the phase angle is given by $\phi = \arctan\frac{B\alpha_1}{\omega}$. The positive/negative sign of a corresponds to supercritical/subcritical Hopf bifurcation, which are both present in the system. Numerical experiments with (3.10) show that typically, for low γ_{T0} values, only supercritical bifurcation occurs, i.e. the bifurcating surge cycle is stable and exists after the bifurcation point. However, for larger γ_{T0} values, a part of the Hopf curve is subcritical, which means that the bifurcating limit cycle is *unstable* and is present *before* the critical parameter values. An example for supercritical bifurcation can be seen in Fig.6(a) at H_2, while the one in e.g. Fig.7(a) at H_1 is subcritical.

3.4 Continuation, Global Bifurcations

Having detected the local bifurcations and the traces of global ones (Takens-Bogdanov point, sign change of the first Lyapunov coefficient), we turn to the numerical continuation techniques implemented in AUTO. Only the most complex two-parameter bifurcation diagram is presented, which occurs when $\gamma_{T0}^{cusp} < \gamma_{T0} < \Psi_C(\Phi_0)$ (see Fig.4). For further numerical study, we fix $H = 0.18$, $W = 0.25$, $\Psi_{C0} = 0.27$, $\Phi_0 = 0.1$ and $\gamma_{T0} = 0.25$ (the value of H and W are the same as those in [11] or [9], Ψ_{C0} is slightly decreased and Φ_0 and γ_{T0} - as new parameters - are chosen freely). The results are shown in Fig.5, details are explained with the help of a horizontal slice $A \to C$ in Fig.6 and a vertical one $D \to E$ in Fig.7. Figures Fig.8-11 depict qualitatively the information in Fig.5 and show the topology of the phase space in each domain. As at the cusp point the two Bogdanov-Takens points merge, this figure series can be considered as the unfolding of a codimension-three bifurcation. The results agree qualitatively with those found in [16], Fig.5/M for a different system of equations (cubic Liénard equations).

Let us describe the curves corresponding to global bifurcations (see Fig.8). At the two Bogdanov-Takens points (TB_1 and TB_2) branches P_1 and P_5 corresponding to homoclinic bifurcations originate (for details, see [19]). At this homoclinic bifurcation, the peiodic orbit born via the Hopf bifurcation reaches the saddle fixed point and becomes an 'infinite-period' limit cycle before disappearing. Branches P_1 and P_5 are globally connected and represent a whole series of homoclinic bifurcations, depicted qualitatively in Fig.11. Another codimension-two bifurcation occurs when the first Lyapunov coefficient (a, defined by (3.10)) changes its sign, which occurs (at this γ_{T0} value) only along H_2. At this so-called Bautin bifurcation point (Ba) a new branch corresponding to cyclic fold bifurcation (FPO_2) arises (see [19]). Passing through such a line as a parameter is varied, *two* periodic orbits are born at once, a stable and an unstable one.

The other cyclic fold (FPO_1) terminates at point NS (indicated only in Fig.8), which is a neutral (or resonant) saddle. This point is strongly related to the Hopf curves H_1 and H_2 as follows. Let us define the saddle quantity concerning to a fixed point through the eigenvalues as $\sigma_0 = \lambda_1 + \lambda_2$. If $\sigma_0 = 0$ and the eigenvalues are purely imaginary, we have a Hopf bifurcation, which holds along H_1 and H_2. As explained in [19] or [3], if the eigenvalues are real, the saddle quantity vanishes and there is a homoclinic orbit around the fixed point, a branch corresponding to fold of periodic orbits originates at this point. (Actually, the homoclinic orbit has to be nontwisted, but this is the only possibility in the plane). Let us consider the surface corresponding to vanishing saddle quantity in the parameter space (γ_T, γ_{T0}, B), which is a cusp-like surface; its projection onto the (γ_{T0}, γ_T) plane is the same as the fold branch in Fig.4 (the *projection* itself is the same, not the 3D surface). For $\gamma_{T0} < \gamma_{T0}^{cusp}$, the curve is a one-to-one surface (branch in H_2 Fig.12) and its whole corresponds to Hopf bifurcation, while beyond the cusp point, the upper and lower 'arm' correspond to the Hopf bifurcation of equilibria $\Phi_e^{(1)}$ and $\Phi_e^{(3)}$ (branches H_1 and H_2 in Fig.8), while the 'middle arm' (S in Fig.11) corresponds to the saddle equilibrium $\Phi_e^{(2)}$.

The practical aspects of the two-parameter bifurcation diagram can be summarized as follows. The presence of FPO_2 indicates that there is a region (denoted by 7 in Fig.9) in which, although linear stability analysis predicts a stable fixed point, it is surrounded by an unstable 'antisurge' cycle and there is a surge cycle 'outside'. In this region, the fixed point is resistant only to perturbations with smaller amplitude then that of the antisurge cycle and the system will begin to surge once the perturbations exceed this amplitude. Hence, linear stability boundaries do not give a reliable picture of the global dynamics.

Concerning the two-parameter bifurcation diagrams, if $\gamma_{T0} < \gamma_{T0}^{cusp}$, we have an (approximately) U-shaped branch of Hopf bifurcations in the (γ_T, B) parameter plane (see branch H_2 in Fig.12(a) and ignore all the other branches plotted there), inside which surge is present. It is clear that for sufficiently small B values, surge can be fully avoided and one can exploit the whole characteristic of the turbomachine. However, for γ_{T0} values slightly less then γ_{T0}^{cusp}, there are two branches corresponding to fold of periodic orbits located similar to those in Fig.5, which reduce the range where the operating point is globally stable.

If three are three possible operating points present in the system, there are two main cases. One of them is present along slice $A \to C$ depicted in Fig.6, where the surge cycle born at H_2 grows quickly but at F_2 it is destroyed by the homoclinic bifurcation and disappears suddenly. Beyond this throttle setting, the system can again operate without surge. In contrast, for larger B values (say, $B = 5$ - see Fig.5), one has to reach curve FPO_1 to obtain surge-free operation.

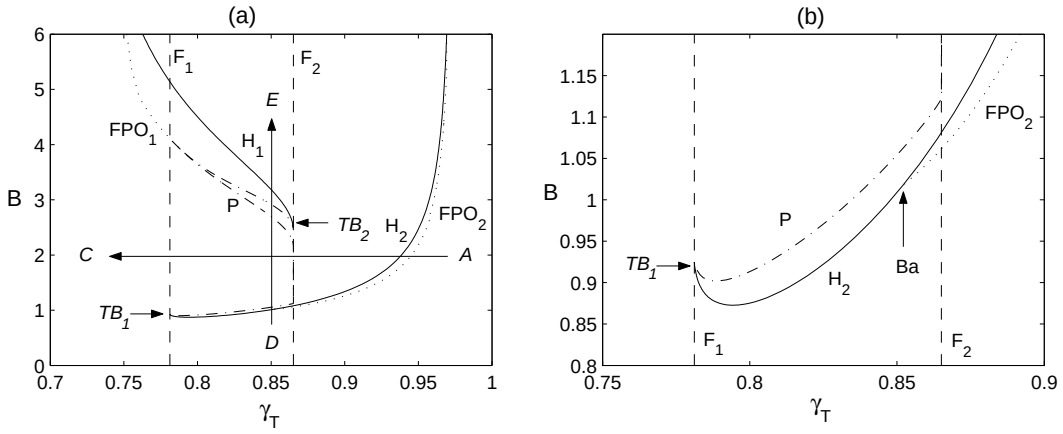

Figure 5: (a) Bifurcation map computed with AUTO. F_1 and F_2 correspond to folds, H_1 and H_2 to Hopf bifurcation, FPO_1 and FPO_2 to folds of periodic orbits, P to homoclinic bifurcation and TB_1 and TB_2 to Takens-Bogdanov points. (b) A zoom close to TB_1. The cuts $A \rightarrow C$ and $D \rightarrow E$ represent the one-dimensional bifurcation diagrams shown in Fig.6 and Fig.7, respectively.

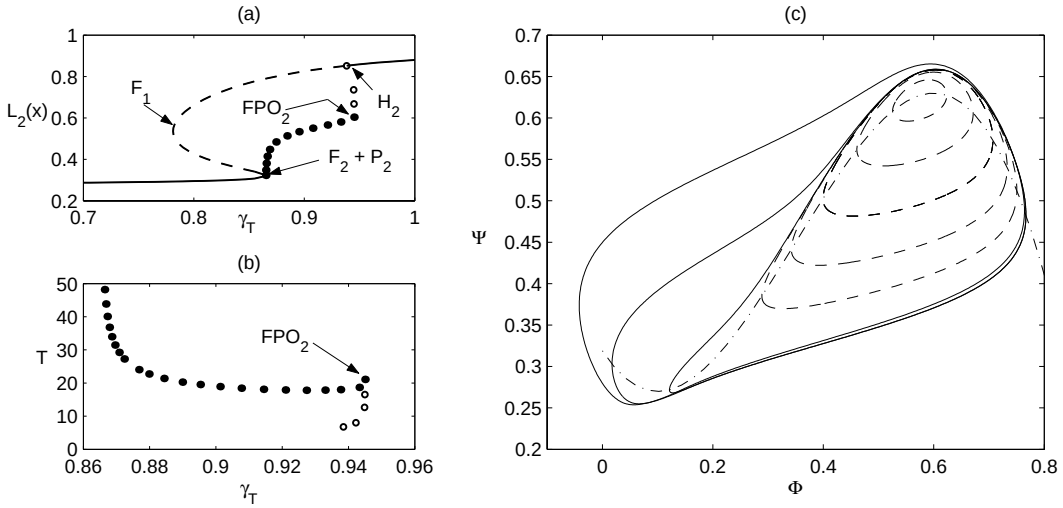

Figure 6: $A \rightarrow C$ transition with $B = 2$. (a) L_2 norm vs. parameter γ_T. Solid lines correspond to stable steady solutions, dashed to unstable ones, filled circles represent stable periodic solutions while empty circles unstable ones. At H_2, a subcritical Hopf bifurcation occurs, the limit cycle changes its stability at FPO_2 and then becomes homoclinic at F_2. (b) Period vs. parameter γ_T, showing the homoclinic nature of the periodic orbit. (c) Phase-space plot of the periodic orbits, the largest one corresponds to the homoclinic orbit. Dashed lines correspond to unstable, solid lines to stable periodic orbits, the dash-dot line represents the compressor characteristic.

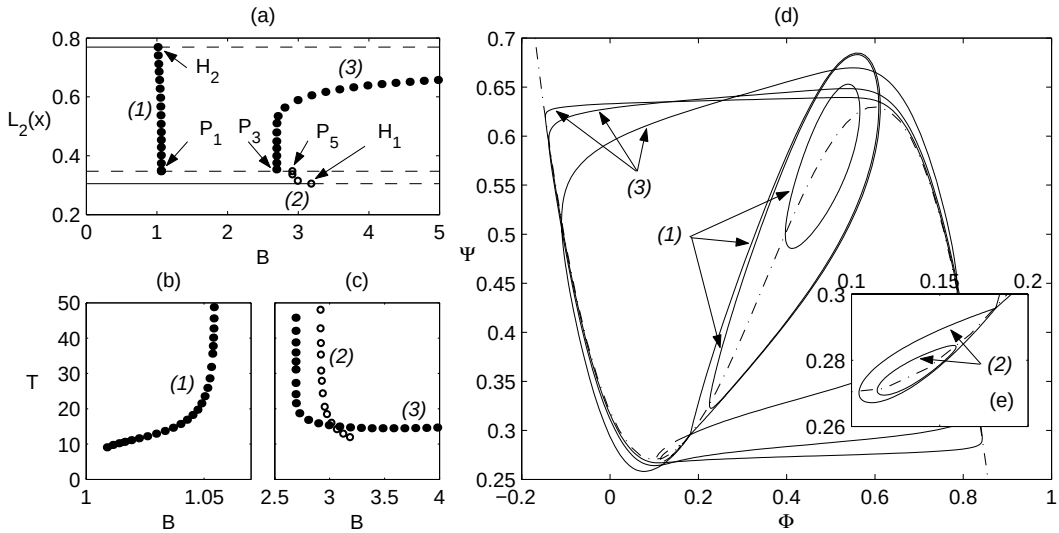

Figure 7: $D \to E$ transition, $\gamma_T = 0.82$. (a) L_2 norm vs. parameter. Starting from the upper-left stable fixed point $L_2(x^{(3)}) = 0.7692$, it loses its stability at H_2 via Hopf bifurcation, the limit cycle born here *(1)* grows rapidly and at P_1, it becomes homoclinic as it reaches the saddle represented by the 'middle' branch, $L_2(x^{(2)}) = 0.3471$. At H_1, the fixed point $L_2(x^{(1)}) = 0.3051$ loses its stability and the limit cycle born *(2)* soon becomes homoclinic at P_5. Deep surge is represented by branch *(3)* which is present for large B values and is destroyed by another homoclinic bifurcation at P_3. (b) and (c) Period vs. parameter, showing the homoclinic nature of all limit cycles. (d) and (e) Phase-space plots, the stability of the limit cycles is not indicated, the compressor characteristic is represented by the dash-dot line.

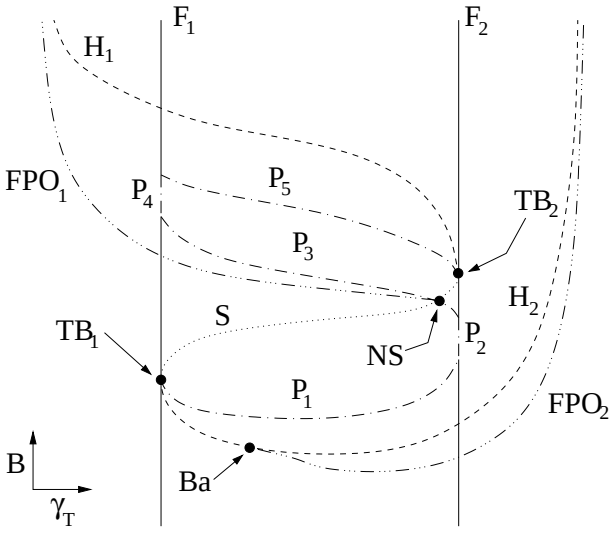

Figure 8: Two-parameter bifurcation diagram, depicted qualitatively. Branches: saddle-node (fold) ($F_{1,2}$), Hopf bifurcation ($H_{1,2}$), fold of periodic orbits (FPO) and homoclinic bifurcations ($P_{1..5}$). Special points: Takens-Bogdanov ($TB_{1,2}$), the origins of the homoclinic series $P_1 \to P_5$, Bautin bifurcation (Ba), where the Hopf bifurcation changes its supercritical/subcritical nature and neutral (resonant) saddle (NS), where FPO_2 originates (see text for details).

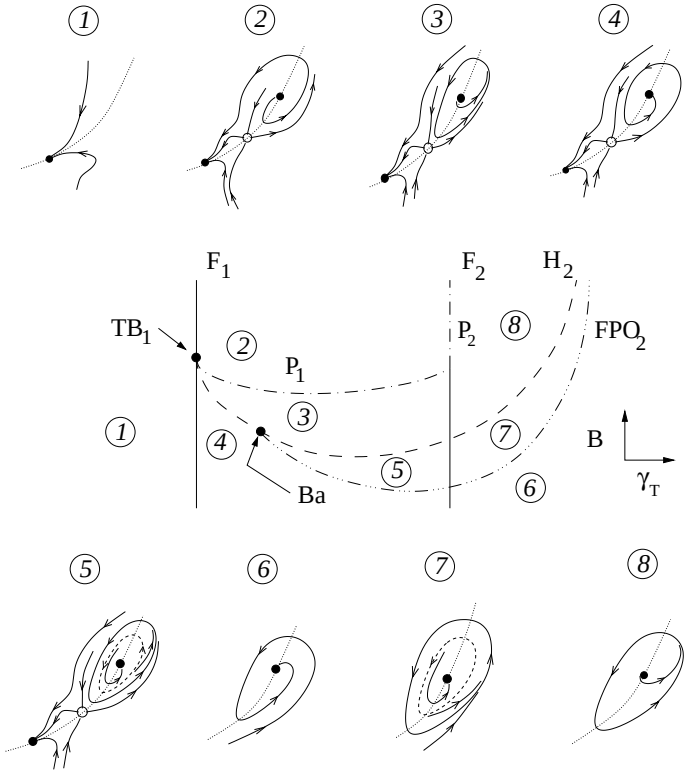

Figure 9: A zoom of Fig.8 close to TB_1. Insets show phase portraits at the numbered regions.

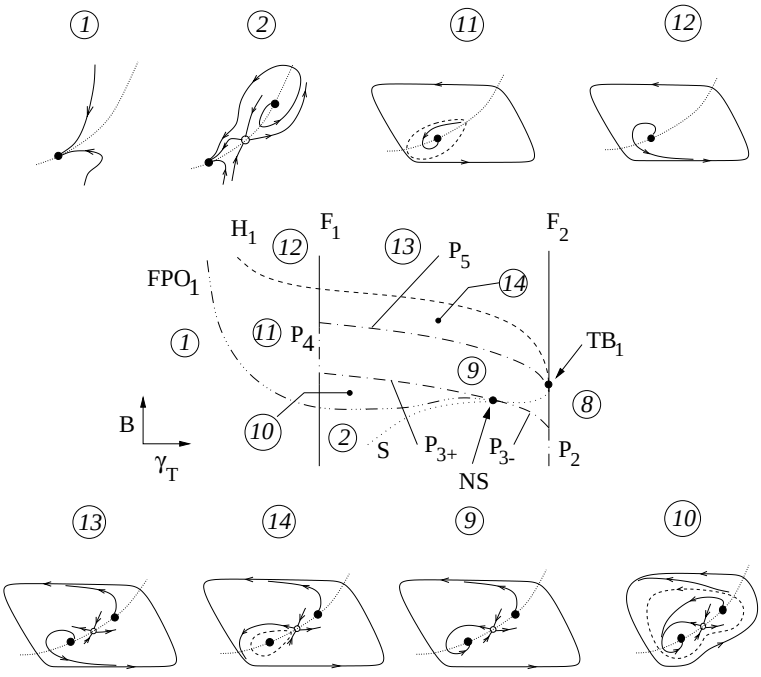

Figure 10: A zoom of Fig.8 near TB_2.

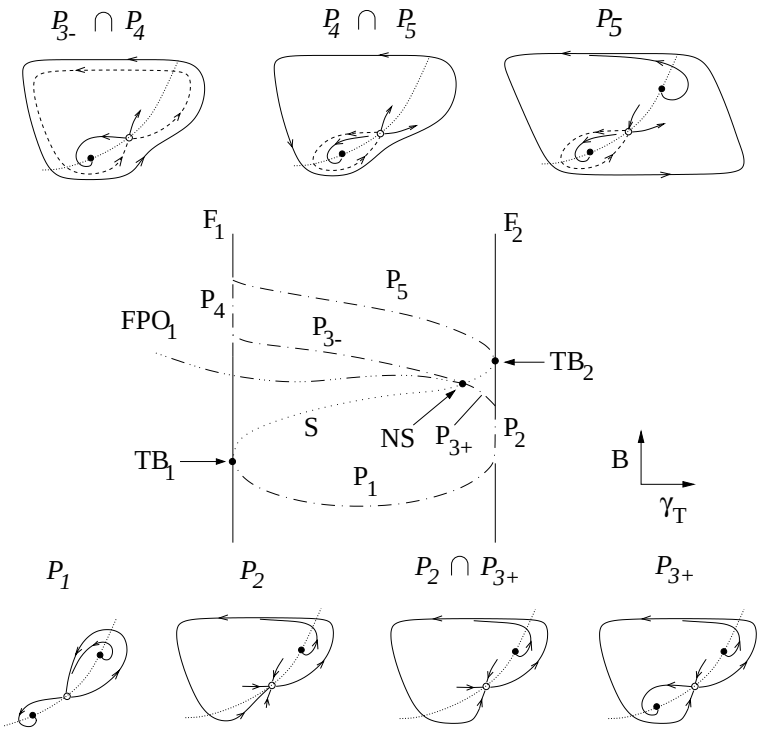

Figure 11: The qualitative depiction of the homoclinic bifurcation scenario.

4 Dynamics in the Presence of Rotating Stall

4.1 Local Stability Analysis

Let us consider system (2.10), with free parameters B and γ_T. To keep the dynamics on the $J = 0$ plane as simple as possible, we set for further calculations $\Phi_0 = 0$ and $\gamma_{T0} = 0$. We begin with the classical local stability theory, determining the stationary points and their bifurcations. As mentioned earlier, system (2.10) has two types of fixed points; rotating stall free (J_e) and rotating-stall fixed points J_e^{RS}. In both cases, the other two components of the equilibria are given by the intersection of the corresponding part of the compressor characteristic and the throttle curve: $\Psi_C(\Phi_e, J_e) = \gamma_T\sqrt{\Psi_e}$. The linear coefficient matrix evaluated at the rotating stall free fixed point yields

$$A(J_e = 0) = \begin{pmatrix} C\alpha_{100} & -C & C\alpha_{001} \\ \frac{C}{4B^2} & -\frac{C}{4B^2\beta_{010}} & 0 \\ 0 & 0 & \rho\delta_{001} \end{pmatrix}, \tag{4.1}$$

where α_{ijk}, β_{ijk} and δ_{ijk} correspond to the linear part of system (2.10). The eigenvalues of the upper-left 2x2 submatrix are the same as those in pure surge mode (see eq.(3.2)), hence, all the results achieved there can be applied here to obtain the dynamics on the invariant $J = 0$ plane. The third eigenvalue $\lambda_3 = \rho\delta_{001}$ governs the dynamics off the plane, which, after simple calculations, turns out to be (assuming for physical relevance $\rho > 0$) repelling in the strip $0 < \Phi_e < 2W$ and attracting outside. The origin $\Phi = 0$ is a Takens-Bogdanov point, while transcritical bifurcation occurs at $\Phi_e = 2W$, where the rotating-stall fixed point crosses the $J = 0$ plane. As fixed points with negative J coordinate have no physical relevance and the $J = 0$ plane is invariant, we can ignore those equilibria below this plane without the danger of missing their influence on the dynamics in the $J > 0$ region.

Symbol	Value	Symbol	Value	Symbol	Value
W	0.25 [−]	γ_{T0}	0.0 [-]	R	0.1 $[m]$
H	0.18 [−]	V	1.5 $[m^3]$	a_s	340 $[\frac{m}{s}]$
Ψ_{C0}	0.27 [−]	A	0.01 $[m^2]$	a	0.3 [−]
Φ_0	0.0 [−]	L	0.8 $[m]$	u,γ_T	free parameter $[\frac{m}{s}]$, [-]

Table 1: Numerical values used in AUTO runs.

At the stalled fixed points, the stability is governed by the eigenvalues of the matrix

$$A(J_e^{RS}) = \begin{pmatrix} C\alpha_{100}^{RS} & -C & C\alpha_{001}^{RS} \\ \frac{C}{4\,B^2} & -\frac{C}{4\,B^2\,\beta_{010}^{RS}} & 0 \\ \rho\delta_{100}^{RS} & 0 & \rho\delta_{001} \end{pmatrix}, \tag{4.2}$$

which can be expressed as the roots of the characteristic equation

$$D(\lambda) = s_0 + s_1\lambda + s_2\lambda^2 + \lambda^3. \tag{4.3}$$

Hopf bifurcation occurs if $s_1\,s_2 = s_0$ and $s_1 > 0$, in which case the eigenvalues are given by $\lambda_{1,2} = \pm i\sqrt{s_1}$ and $\lambda_3 = -s_2$. Although one can give analytical conditions for bifurcations, the resulting formulae are cumbersome to handle and do not provide an insight into the dynamics. Hence, we turn to numerical techniques to obtain bifurcation diagrams.

4.2 Global Bifurcations, Numerical Results

The parameter values used in AUTO computations are shown in Table 1 and are taken from Appendix D in [9], apart from Ψ_{C0}, which is slightly changed for numerical convenience, although taking the true value of 0.3 was found to make little qualitative difference. The rotor rotation speed u and the throttle setting γ_T were chosen as free parameters to vary, the former implies that all the coefficients B, C, ρ in system (2.10) change simultaneously (we dropped the tilde on B). All the results were rescaled to show the bifurcation branches in terms of B instead of u (i.e. simply $B \approx 0.02014\,u$). The results of the two-parameter bifurcation analysis are shown in Fig.12, detailed explanation is given with the help of two representative slices; at $B = 0.8055$ (i.e. $u = 40$) in Fig.13 and at $B = 1.0069$ ($u = 50$) in Fig.16. Before launching into a careful description of these bifurcation diagrams, it is to be emphasized that the two-parameter bifurcation diagram is far from complete and only those branches are shown that correspond to global qualitative change in the dynamics.

Let us now describe the bifurcation diagrams in detail. In Fig.12, there are three branches of Hopf bifurcations: H_2 corresponds to the bifurcation of the rotating stall-free equilibrium (the surge cycle on the plane is born when crossing this line) while H_1 and H_3 correspond to the rotating stall equilibrium. The dashed line F indicates saddle-node bifurcation, where two new fixed points are born (x_{02} and x_{03} in Fig.2). Upon decreasing γ_T, x_{03} approaches x_{01} and merges with it at T_{FP}, then crosses the $J = 0$ plane and leaves towards the $J < 0$ region, which we are not interested in. This transcritical bifurcation of fixed points (T_{FP}) is located at $\Phi_e = 2\,W$ ($\gamma_T \approx 0.63$), which is the local maximum of the compressor characteristic. At this point, the rotating stall free fixed point x_{01} loses its stability and becomes repelling off the plane, while remains stable in the $J = 0$ the plane. Corresponding to the other fixed point x_{02} born at F, there are two different scenarios. If we are below the B value corresponding to Takens-Bogdanov bifurcation (i.e. $B < B^{TB}$), a stable rotating stall equilibrium is born. If $B > B^{TB}$, this fixed point is born with one stable and two unstable directions and then regains its stability via the Hopf bifurcation at H_1. According to global bifurcations, a branch of homoclinic orbits P originates at TB and a transcritical of periodic orbits (T_{PO}) was found when computing the periodic orbits born along H_2.

In Fig.13, the one-parameter bifurcation diagram is plotted for fixed B value 0.8055. Here, Hopf bifurcation H_1 is subcritical, the periodic orbit changes its stability at FPO and then undergoes a series of folds of periodic orbits bifurcations (see panel (b)). This branch - *(3)* - terminates at $T_{FP} + P$, which means that it becomes a homoclinic orbit to a fixed point, which is a stable focus on the $J = 0$ plane and neutral in the normal direction. This homoclinic orbit plays a central role in the birth of classic surge, i.e. a

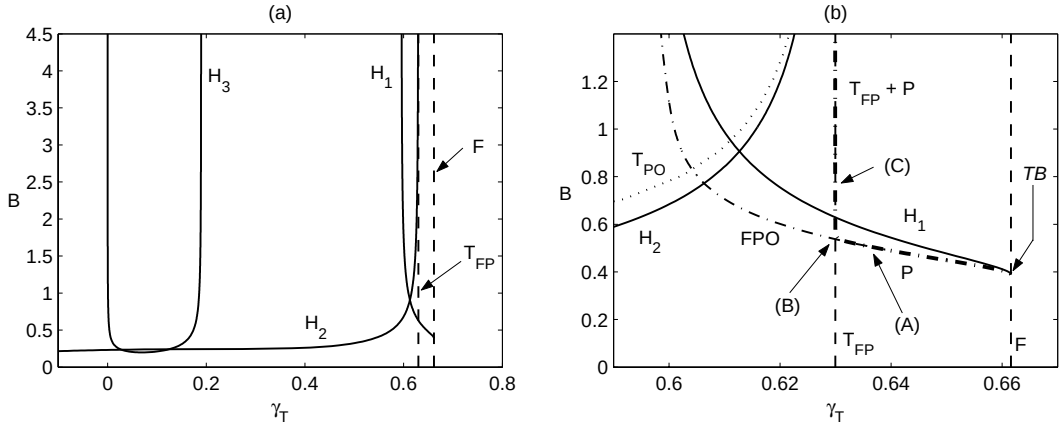

Figure 12: Two-parameter bifurcation diagram computed with AUTO. (a) Greitzer's B parameter vs. throttle setting γ_T. Only the branches corresponding to Hopf bifurcation (H_1, H_2 and H_3), fold (F) and transcritical of fixed points (T_{FP}) are shown. (b) A zoom close to the Takens-Bogdanov point TB also showing the homoclinic branch (P), the fold of periodic orbits (FPO) and the transcritical bifurcation of periodic orbits (T_{PO}).

γ_T	Dynamics
$0 \rightarrow H_3$	deep surge
$H_3 \rightarrow T_{PO}$	deep surge + rotating stall
$T_{PO} \rightarrow FPO$	rotating stall
$FPO \rightarrow H_1$	rotating stall + classic surge
$H_1 \rightarrow T_{FP}$	classic surge
$T_{FP} \rightarrow$	stable axisymmetric flow

Table 2: Qualitative classification of global dynamics at $B = 0.8055$.

combined surge-stall cycle. In Fig.14, three of these homoclinic orbits are plotted along curve P to explain the mechanism of the birth of the classic surge cycle. Orbit *(A)* is an unstable periodic orbit born at H_1, which is homoclinic to the saddle-node x_{03}. As x_{03} approaches the plane along P (moving to the left of *(A)* in Fig.12), so does the homoclinic orbit, and at $P \cap T_{FP}$ it reaches the plane (orbit *(B)* in Fig.14). From this point, the homoclinic curve P is 'glued' to the T_{FP} line and moves 'upwards'. Along this segment of P, the homoclinic orbit becomes more and more twisted (as the fixed point is a stable *focus* on the plane). One of these twisted stable periodic orbits close to the homoclinic was found along branch *(3)* at $B = 0.8055$ (Shil'nikov-like homoclinic orbit to an equilibrium undergoing a transcritical bifurcation). Note that we are not aware of any previous work that studies such a bifurcation scenario, but see the work of Deng [6] for related cases. For the unstable limit cycle *(2)* born at H_3 in Fig.13, continuation reveals that it comes together with the surge cycle *(1)* at T_{PO} and then leaves to the $J < 0$ region. The surge cycle on the plane becomes stable (H_2 is subcritical bifurcation) via this codimension-one transcritical bifurcation of periodic orbits T_{PO}. The global classification of the dynamics is shown in Table 2 while time histories of the transition from surge to the combined cycle are shown in Fig.15.

In Fig.16, another one-parameter slice of the parameter plane is plotted, at $B = 1.0069$ ($u = 50$). Note that branch *(2)* does not terminate at T_{PO}, but at H_1 and, on the other hand, branch *(3)* is not born at H_1, but originates at T_{PO}. This means that there has been a codimension-two transcritical bifurcation of limit cycles between parameters $u = 40$ and $u = 50$. Due to the 'wiggling' of branch *(3)*, the location of this bifurcation was determined only approximately and was found to be at ($\gamma_T^* \approx 0.604, B^* \approx 0.83$). This bifurcation has a fundamental effect on the presence of classic surge; in contrast to the previous slice ($u = 40$), where the presence of classic surge was bounded by FPO and T_{FP}, in this case, it is present

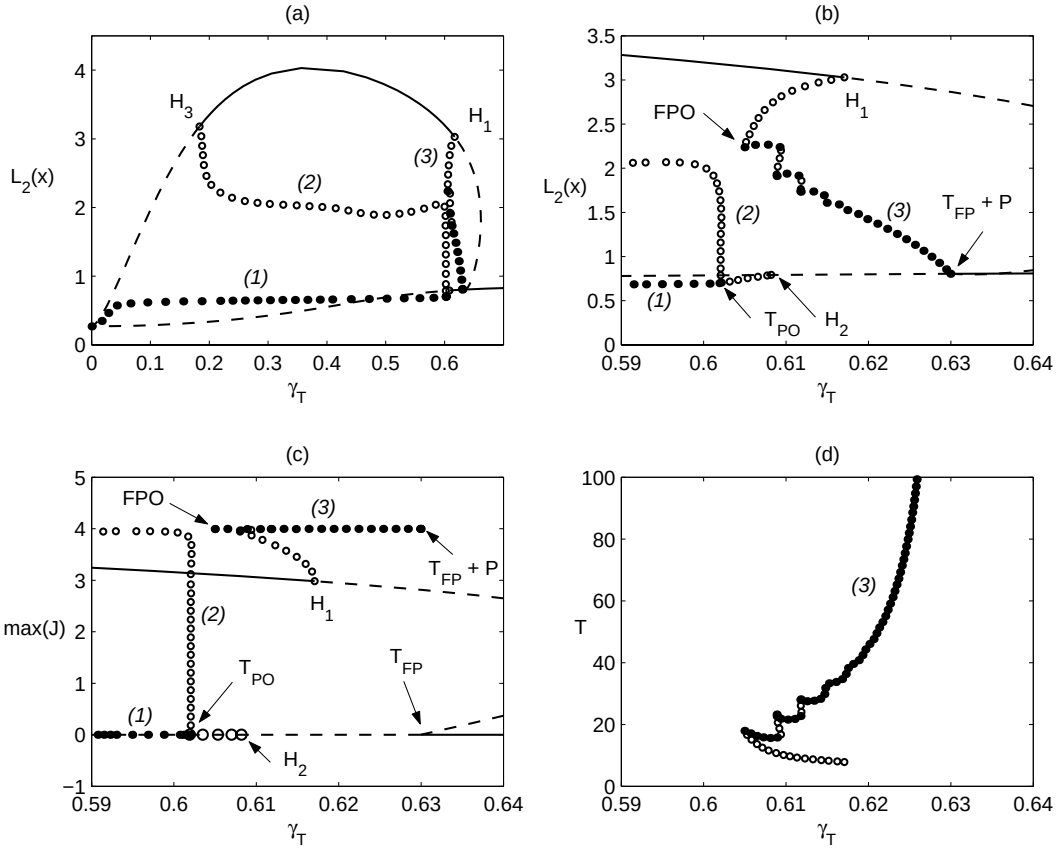

Figure 13: One-parameter bifurcation diagram at $B = 0.8055$ ($u = 40$). (a) L_2 norm vs. parameter. (b) A zoom showing the birth and death of the classic surge cycle (branch *(3)*). (c) max(J) vs. γ_T. Note that although the L_2 norm of branch *(3)* tends to the fixed point in panel (b), the maximum of the J component remains large. Thus, along a classic surge cycle, rotating stall fully develops and dies away. (d) Period T vs. parameter, showing the homoclinic nature of the classic surge cycle.

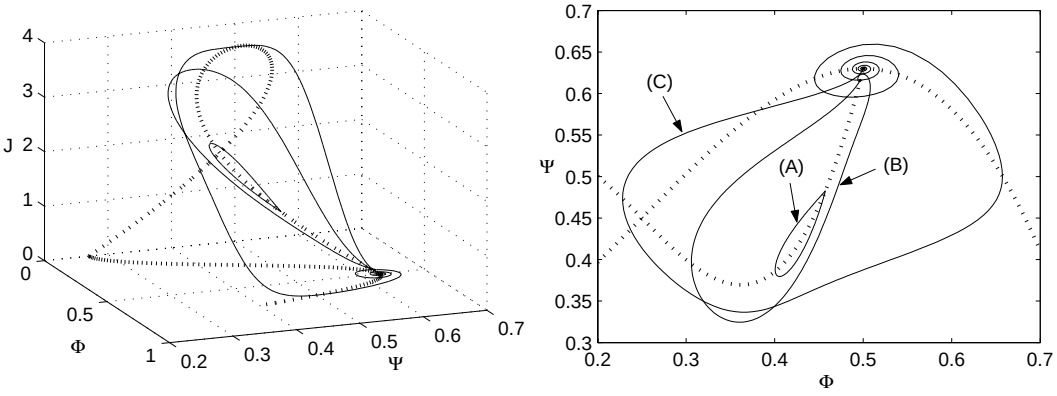

Figure 14: Birth of the classic surge cycle: (A) homoclinic orbit to saddle-node fixed point, (B) homoclinic orbit to the non-hyperbolic fixed point at $P \cap T_{FP}$ and (C) homoclinic orbit to the non-hyperbolic fixed point. (Corresponding parameter values are indicated in Fig.12).

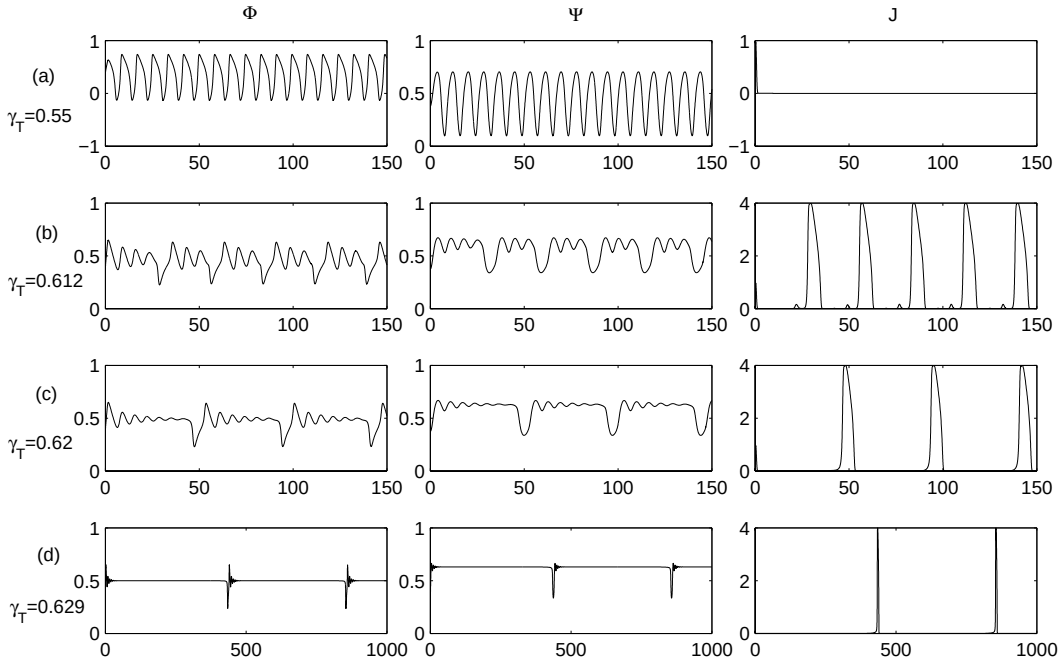

Figure 15: Transition from deep surge to classic surge (B=0.8), note the different time scales between panel (a)-(c) and (d).

between T_{PO} and T_{FP}. For a qualitative depiction of this bifurcation scenario, see Fig.17.

Having completed the bifurcation analysis, let us turn to the engineering interpretation. The results clearly explain the huge deep surge/rotating stall hysteresis in the 'middle' region (approx. $0.2 < \gamma_T < 0.6$); which is a large-amplitude unstable limit cycle - branch *(2)* - around the rotating stall fixed point. In this region, depending on the initial conditions, the system goes either into stall or deep surge. A first-order approximation of the attracting domain of rotating stall could be given using centre manifold restriction techniques.

There are also other hysteresis effects found in the system. For example, rotating stall/classic surge hysteresis is present e.g. at $B = 0.8055$, if $FPO < \gamma_T < H_1$ (see Fig.13), but this region is practically narrow enough to neglect. Similarly, if $T_{FP} < \gamma_T < F$, then between H_1 and P (see in Fig.12) rotating stall is locally stable, there exists an unstable limit cycle around it and the stall-free fixed point (uniform, axisymmetric flow) is stable as well. However, the amplitude of this unstable limit cycle is so small, that the attracting region of the stalled fixed point is practically zero.

Although all the branches are needed to keep the dynamics topologically consistent, only a few of them have a *robust* effect on the global dynamics. For example, the surge cycle becomes stable and hence, appears in experiments at T_{PO} and not at H_2, but the distance between the two curves is so small that it may be missed even by the most carefully conducted experiments.

These observations coincide with the experimental results published in [11] as presented in Fig.18. As Greitzer used the equilibrium mass flow rate as a bifurcation parameter, we have to transform Fig.12 into this system as well. This means simply that no matter what kind of fixed point a branch corresponds to (x_{01}, x_{02} or x_{03}), we replace its γ_T coordinate by the fixed point corresponding to uniform flow at the same γ_T value, i.e. x_{01}. We also neglect those curves which were found not to have a robust effect on the global dynamics. The size of the various regions are also different (Fig.18(a) is a zoom close to T_{PO} while panel (b) shows the whole range of throttle settings), which is due to the different shape of compressor characteristics. However, by and large, we are left with an excellent qualitative accordance between theory and measurements, as already noticed by McCaughan in [21], who only depicted the Hopf curves. This proves that the Greitzer-Moore ODE system for modelling surge and rotating stall captures the dynamics qualitatively on a global scale and

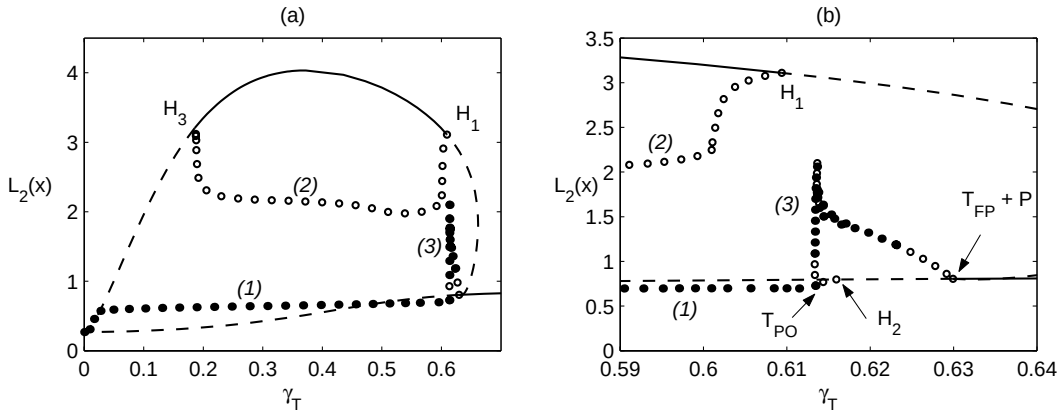

Figure 16: One-parameter bifurcation diagram at B=1.0069 (u=50). (a) L_2 norm vs. parameter. Note that branch *(2)* terminates at H_1 and branch *(3)* is born at T_{PO}, unlike in Fig.13. (b) A zoom showing the classic surge cycle.

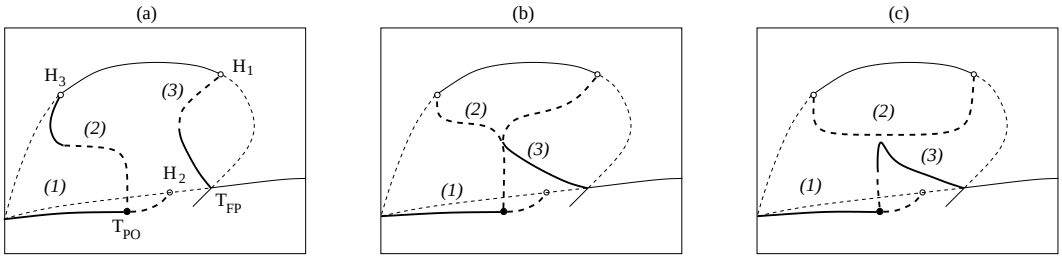

Figure 17: The qualitative depiction of the codimension-two transcritical bifurcation of periodic orbits scenario. Numerical results corresponding to (a) and (c) are shown in Fig.13 and Fig.16, respectively.

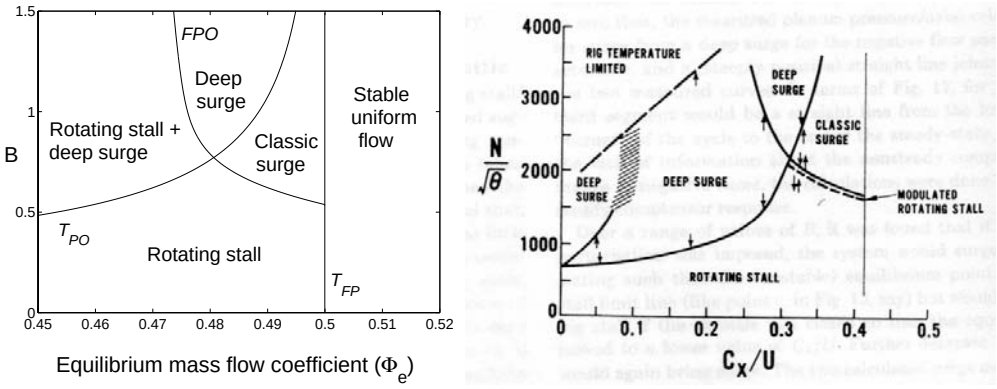

Figure 18: (a) 'Practical' two-parameter bifurcation diagram showing the response boundaries of the system. (b) Experimentally determined map of parameter space, taken from [11].

includes the explanation of all the different modes of vibrations encountered in laboratory experiments.

5 Conclusions

This study has presented a detailed investigation of the Greitzer-Moore ODE system for modelling surge and rotating stall. Special attention was paid to global bifurcations, which were detected and followed with the help of the continuation software AUTO. It was found that these complex bifurcation scenarios should be included in order to gain a full understanding of the dynamics and to predict the various parameter ranges where surge, rotating stall and classic surge are present. In the case of pure surge, the stable domain obtained by linear stability analysis may be further reduced due to the presence of an 'antisurge' cycle around the stable operating point. In contrast, if there are several fixed points, the surge cycle may die away before it is fully grown, hence, a larger segment of the turbomachine characteristic might be exploited. The origin of the classic surge cycle was found to be a highly non-trivial Shil'nikov-like periodic orbit to a non-hyperbolic equilibrium located in an invariant plane. The parameter boundaries of deep surge, rotating stall and classic surge described experimentally by Moore and Greitzer [22] and mathematically by McCaughan in [21] were further refined in terms of global bifurcation theory.

An interesting topic for future work would be to give an explanation of the 'wiggles' of branch *(3)* in Fig.13 and to detect accurately the codimension-two transcritical bifurcation of periodic orbits. Also, a better understanding of the Shil'nikov-to-transcritical bifurcation may provide new insights into the dynamics of the system. Including more Galerkin modes may result in complex dynamical systems but also may describe rotating stall in details (e.g. the rotation of the stalled cells is completely neglected in this model). Also, the presence of the Shil'nikov-like orbit suggests that there might be other, highly non-trivial global attractors present in the system.

From a more practical point of view, industrial facilities (as e.g. air conditioning systems) include numerous elements, hence building a mathematical model of them may result in large ODE systems. It would be interesting to explore whether the domain of stable operation might be determined in a similar way and whether centre manifold restriction techniques give a reliable approximation to the appearing surge cycles. Real-life compressor characteristics could be used in computations in order to validate the described phenomena, which would also require techniques to predict the *whole* unstalled segment. Also, the robustness of the bifurcation phenomena is an open question, i.e. how do different turbomachine characteristics influence the existence and location of the bifurcation branches. A further step would be to study control techniques in the light of *global* bifurcation theory and try to implement the results into industrial applications.

6 Acknowledgments

Cs. Hős would like to thank professor G. Stépán, corresponding member of the Hungarian Academy of Sciences for all his encouragement and support. Part of this work has been completed while Cs. Hős was visiting the University of Bristol, Department of Engineering Mathematics, which has been financially supported by the Hungarian Eötvös Scholarship and the Magyar Mérnökakadémia Alapítvány - Rubik Nemzetközi Alapítvány.

References

[1] E.H. Abed, P.K. Houpt, and W.M. Hosny. Bifurcation analysis of surge and rotating stall in axial flow compressors. Technical Report TR 90-27r2, University of Maryland, System Research Center, 1990.

[2] R.A. Adomaitis, D-C. Liaw, and E.H. Abed. Nonlinear dyamics of axial-flow compressors: A parametric study. Technical Report TR 92-73, University of Maryland, System Research Center, 1992.

[3] A.R. Champneys and Yu.A. Kuznetsov. Numerical detection and continuation of codimension-two homoclinic bifurcations. *International Journal of Bifurcation and Chaos*, 4(4):785–822, 1994.

[4] X. Chen, G. Gu, P. Martin, and K. Zhou. Rotating stall control via bifurcation stabilization. *Automatica*, 34(4):437–443, 1998.

[5] N.A. Cumpsty. *Compressor Aerodynamics*. Longman, 1989.

[6] B. Deng. Homoclinic bifurcations with nonhyperbolic equilibria. *SIAM Journal of Mathematical Analysis*, 21:693–719, 1990.

[7] E.J. Doedel, T.F. Fairgrieve, B. Sandstede, A.R. Champneys, Y.A. Kuznetsov, and X. Wang. Auto97: Continuation and bifurcation software for ordinary differential equations. `http://indy.cs.concordia.ca/auto`, 1999.

[8] A.H. Epstein, J.E.F. Williams, and E.M. Greitzer. Active suppression of aerodynamic instabilities in turbomachines. *J.Propulsion*, 5:204–211, March-April 1989.

[9] J.T. Gravdahl. *Modeling and Control of Surge and Rotating Stall in Compressors*. PhD thesis, Department of Engineering Cybernetics, NTNU, 1998.

[10] J.T. Gravdahl, F. Willems, de Jager, and O. Egeland. Modeling for surge control of centrifugal compressors: comparison with experiment. In *Proceedings of the 39th IEEE Conference on Decition and Control*, volume 2, pages 1341–1346, December 2000.

[11] E.M. Greitzer. Surge and rotating stall in axial flow compressors, part 1,2. *Transactions of the ASME, Journal of Engineering for Power*, 98:190–217, April 1976.

[12] E.M. Greitzer. Review - axial compressor stall phenomena. *Transactions of ASME, Journal of Fluids Engineering*, 102:134–151, June 1980.

[13] G. Gu, A. Sparks, and S.S. Banda. An overview of rotating stall and surge control for axial flow compressors. *IEEE Transactions on Control System Technology*, 7(6):639–647, November 1999.

[14] J. Guckenheimer and P. Holmes. *Nonlinear Oscillations, Dynamical Systems, and Bifurcations of Vector Fields*. Springer-Verlag, 1983.

[15] W.M. Haddad, A. Leonessa, W-S. Chellaboina, and J.L. Fausz. Nonlinear robust disturbance rejection controllers for rotating stall and surge in axial flow compressors. *IEEE Transactions on Control Systems Technology*, 7(3):391–398, May 1999.

[16] A.I. Khibnik, B. Krauskopf, and C. Rousseau. Global study of a familiy of cubic Lieńard equations. *Nonlinearity*, 11:1505–1519, 1998.

[17] L. Kullmann and T.H. Carolus. Theoretical and experimental determination of surge in fan systems. In *Proceedings of the 7th Conference on Fluid Machinery*, volume 111, June 1983.

[18] L. Kullmann and T.H. Carolus. Pumpschwingungen in einer Lufttechnischen Anlage: Vergleich zweier Rechenmodelle Anhand Experimentelle Ergebnisse. *Periodica Polytechnica Electrical Engineering*, 29(2-4):169–188, 1985.

[19] Yu.A. Kuznetsov. *Elements of Applied Bifurcation Theory*. Springer-Verlag, 1998.

[20] D-C. Liaw and E.H. Abed. Active control of compressor stall inception: a bifurcation-theoretic approach. *Automatica*, 32(1):109–115, 1996.

[21] F.E. McCaughan. Bifurcation analysis of axial flow compressor stability. *SIAM Journal on Applied Mathematics*, 50(5):1232–1253, October 1990.

[22] F.K. Moore and E.M. Greitzer. A theory of post-stall transients in axial compression systems: Part 1. *Transactions of the ASME, Journal of Engineering for Gas Turbines and Power*, 108:68–76, January 1986.

[23] Y. Wang and R.M. Murray. Bifurcation control of rotating stall with actuator magnitude and rate limits: part 1,2. *Automatica*, 38:597–625, 2002.

[24] M. Xiao and T. Basar. Center manifold of the viscous Moore-Greitzer PDE model. *SIAM Journal of Applied Mathematics*, 61(3):855–869, 2000.

List of Figures

List of Tables